# Hall mobilities and sheet carrier densities in a single $LiNbO_3$ conductive ferroelectric domain wall

Henrik Beccard,[1] Elke Beyreuther,[1,*] Benjamin Kirbus,[1] Samuel D. Seddon,[1] Michael Rüsing,[1,2] and Lukas M. Eng[1,3]

[1] *Institute of Applied Physics, Technische Universität Dresden, Nöthnitzer Straße 61, 01187 Dresden, Germany*

[2] *Integrated Quantum Optics, Institute for Photonic Quantum Systems (PhoQS), Paderborn University, 33098 Paderborn, Germany*

[3] *ct.qmat: Dresden-Würzburg Cluster of Excellence—EXC 2147, Technische Universität Dresden, 01062 Dresden, Germany*

(Received 2 August 2023; revised 3 November 2023; accepted 17 November 2023; published 26 December 2023)

In the last decade, conductive domain walls (CDWs) in single crystals of the uniaxial model ferroelectric lithium niobate ($LiNbO_3$; LNO) have been shown to reach resistances more than 10 orders of magnitude lower than the resistance of the surrounding bulk, with charge carriers being firmly confined to sheets with a width of a few nanometers. LNO is thus currently witnessing increased attention because of its potential in the design of room-temperature nanoelectronic circuits and devices based on such CDWs. In this context, the reliable determination of the fundamental transport parameters of LNO CDWs, in particular the 2D charge carrier density $n_{2D}$ and the Hall mobility $\mu_H$ of the majority carriers, is of great interest. In this contribution, we present and apply a robust and easy-to-prepare Hall-effect measurement setup by adapting the standard four-probe van der Pauw method to contact a single, hexagonally shaped domain wall that fully penetrates the 200-μm-thick LNO bulk single crystal. We then determine $n_{2D}$ and $\mu_H$ for a set of external magnetic fields $B$ and prove the expected cosinelike angular dependence of the Hall voltage. Lastly, we present photoinduced-Hall-effect measurements of one and the same DW, by determining the impact of super-band-gap illumination on $n_{2D}$.

DOI: 10.1103/PhysRevApplied.20.064043

## I. INTRODUCTION

Continuous progress in solid-state nanotechnology relies on answering a number of unsolved scientific questions with respect to both material systems and device operation principles. One such burning issue is electrical transport under well-defined and controlled conditions in reduced dimensions, as in 2D-material systems. While, for example, 2D van der Waals materials have been thoroughly analyzed [1], our focus here is on 2D sheets built up from ferroelectric conductive domain walls (CDWs), i.e., the transition regions between ferroelectric domains of opposite dielectric polarization, which can be tuned to exhibit a strongly enhanced conductivity as compared with the surrounding bulk [2,3]. DWs in ferroelectrics have been reported to form effective 2D electron gases after application of specialized preparation routines to these wide-band-gap bulk materials [4,5]. $LiNbO_3$ (LNO) turned out to be *the* "*Drosophila*" ferroelectric for CDW engineering, since it is robust, semiconductor compatible, and easy to reconfigure at room temperature, while being commercially available both as a bulk material and in crystalline thin-film-on-insulator form [6–9]. Notably, this ever-increasing interest in CDWs has been reviewed with respect to both theoretical and device-oriented aspects [10–17].

At the fundamental level, primarily, the divergence of the ferroelectric polarization (i.e., the local vector field that describes the volume density of unit-cell dipoles) at the DW has been identified as one of the main driving forces behind the localized DW conductivity that was predicted in the 1970s [18]. This divergence is understood as an intrinsic charge density acting as the source of the so-called depolarization field. In turn, the emergent electrostatic field leads to the attraction of free charge carriers to the DWs, as well as to the population of otherwise free electron and/or hole states due to local band bending at the DW position. For the simplest case of a uniaxial ferroelectric (as is LNO) that shows purely Ising-type DWs, this divergence is directly related to the geometrical inclination of the DW with respect to the polar axis [2,19].

Nevertheless, on a practical level, the determination of DW-related quantitative transport data such as the charge carrier type, density, and mobility, has been, to date,

*elke.beyreuther@tu-dresden.de

 

restricted to a few exemplary cases. In this context, especially the analysis of the Hall effect in DWs in the improper ferroelectrics $YbMnO_3$ and $ErMnO_3$ has been shown to be a valuable tool, as reported in the groundbreaking papers of Campbell *et al.* [20] and Turner *et al.* [21], respectively. Those authors chose scanning-probe-based approaches for the evaluation, needing a cumbersome and sophisticated procedure to disentangle the Hall potential from the cantilever-based three-terminal reading via calibration routines and accompanying simulations. Moreover, as those authors stated, their approach is valid mainly for extraction of near-surface charge-carrier densities and mobilities. With respect to proper ferroelectrics, the Hall-effect investigation by Qian *et al.* [22] of DW *p*-*n* junctions engineered into *x*-cut thin-film lithium niobate was equally limited to near-surface carrier densities, while McCluskey *et al.* [23] made use of the fact that a DW in *z*-cut thin-film-lithium-niobate is comparable to the Corbino-cone geometry and in turn found promisingly high carrier mobilities, which were extracted from a magnetoresistance analysis. Notably, Beccard *et al.* [5] recently proposed a completely different approach, quantifying the 2D charge-carrier densities $n_{2D}$ and Hall mobilities $\mu_H$ through "macroscopic" Hall-effect measurements by adapting the classical van der Pauw (vdP) [24] four-point electrode configuration to measurements from a single CDW in bulk $BaTiO_3$.

The work presented in this paper starts similarly as the approach in Ref. [5], by adopting the vdP scenario to the particular case of a single CDW in *z*-cut bulk $LiNbO_3$, the uniaxial model ferroelectric of uttermost importance for prospective nanoscale applications. While significantly high DW conductivity (DWC) in LNO has been proven in the last decade in a number of consecutive studies [2,3,25,26], Hall-effect measurements in LNO CDWs are still lacking. The challenge consists in adapting the vdP method to the hexagonally shaped DW in LNO as depicted in Fig. 1; as seen, the four vdP contacts then likely measure the parallel junction of two such conductive DWs in LNO, rather than connecting to one single planar 2D sheet as was the case for the CDW in $BaTiO_3$ [5]. Nonetheless, in the following we show that evaluating the DW sheet resistance and the magnetic-field-dependent Hall voltages still allows application of the vdP method, hence revealing quantitative data for both $n_{2D}$ and $\mu_H$ on a so-far-unprecedented level and with so-far-unprecedented precision. The error stemming from the parallel DW junction is a factor of 2 at maximum, as easily figured by calculating the total resistance of a parallel junction of two identical or two different resistors, i.e., two CDWs. Notably, this factor of 2 does not change the order of magnitude of $n_{2D}$ and $\mu_H$. In addition, the same error factor of 2 is obtained when the Hall data are analyzed in a more-rigorous way by application of the concept of the resistor network [27], as is discussed in Sec. D in Supplemental Material [28].

Moreover, the integrity of the results obtained by the vdP method is corroborated here by two further investigations: (i) by our quantifying the angular Hall-voltage dependence, and (ii) by our inspecting the Hall-voltage response under super-band-gap illumination for the purpose of generating additional electron-hole pairs within the CDW.

## II. MATERIALS AND METHODS

### A. Samples: Fabrication of domain walls

We used two 5 mol% Mg–doped congruent *z*-cut $LiNbO_3$ crystal plates, with sizes of approximately $1 \times 0.5$ mm$^2$ in the *x*-*y* plane and a thickness of 200 μm in the polar *z* direction, which were cut from a commercial wafer obtained from Yamaju Ceramics Co., Ltd. In the following, we label these samples as "$LNO_1$" and "$LNO_2$." A single, fully penetrating and hexagonally shaped ferroelectric domain of 257-μm-diameter ($LNO_1$) and 356-μm-diameter ($LNO_2$) [see Figs. S7(a) and S7(b) in the Supplemental Material [28]] was then grown into these samples by our applying the well-established method of UV-assisted poling [25,29] using liquid electrodes and a He-Cd laser (Kimmon Koha IK3301R-G) operated at a wavelength of 325 nm; for more details, see, e.g., Refs. [25,30]. Then, four 8-nm-thick chromium electrodes were vapor-deposited in high-vacuum conditions onto every DW structure, with use of a shadow mask. The exact electrode geometry and arrangement with respect to the two crystals and DW orientations are sketched in Figs. 1(b) and 1(d), while a polarization-sensitive-microscopy top-view image is shown in Fig. S7(c) in Supplemental Material [28]. In the following, the electrodes are consecutively labeled by indices 1–4, as is standard in four-point van der Pauw experiments. As a result, the four vdP electrodes, 1–4, directly contact the two DWs that lie in the *x*-*z* plane, one at the front (dashed red line) and one at the back (dotted green line), as seen in Fig. 1 for $LNO_1$ and $LNO_2$, respectively. Note that in parallel, two monodomain reference samples, $LNO_3$ and $LNO_4$, were prepared as well, having identical electrodes 1–4 but containing no DWs.

### B. Enhancement of the domain-wall conductivity

Subsequently, the as-grown hexagonal DWs in $LNO_1$ and $LNO_2$ underwent the DWC-"enhancement" procedure by our applying high voltages between the $z^+$ and $z^-$ sides supplied by the voltage source of a Keithley 6517B electrometer, as described in Refs. [2,3]. The corresponding current-voltage curves recorded during these voltage ramps are depicted in Fig. S1 in Supplemental Material [28], and the exact parameters of the postgrowth treatment are given in Table S1 in Supplemental Material [28]. Our enhancement procedure leads to higher average DW inclination angles relative to the polar *z* axis and, in turn, to

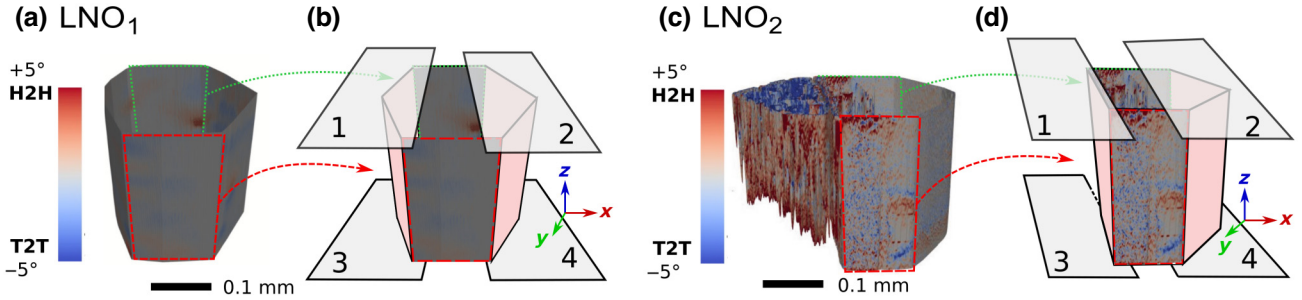


FIG. 1. (a),(c) Three-dimensional-CSHG-microscopy data and (b),(d) chromium-electrode arrangement 1–4 for the two samples $LNO_1$ and $LNO_2$ as prepared from $z$-cut $LiNbO_3$ single crystals for Hall-transport measurements using the van der Pauw method. Note that contacts 1–4 enclose a parallel junction of two CDWs, one at the front (dashed red line) and one at the back (dotted green line). The different protocols applied for DWC enhancement in $LNO_1$ [(a),(b)] and $LNO_2$ [(c),(d)] resulted in the different shapes and appearances as seen in (a),(c). The enhanced and desired head-to-head (H2H) DW inclination is color coded in red in the CSHG scale bar, while tail-to-tail- (T2T) type DWs appear in blue. As seen, sample $LNO_2$ shows a larger DW inclination enhancement, justifying the larger DW current, as compared with sample $LNO_1$.

stronger DW-confined charge accumulation and thus to a larger DW conductivity. However, to possibly break up the initial parallel DW junction arrangement (see Fig. 1) and to apply our Hall-effect measurements to a single CDW, the enhancement procedure here was realized differently and deliberately asymmetrical for the two LNO samples. In particular, we treated $LNO_1$ with only one high-voltage ramp between electrodes 1 and 3, while $LNO_2$ experienced consecutive voltage ramps between both top-bottom electrode pairs 1-3 and 2-4, respectively; see Table S1 and Fig. S1 in Supplemental Material [28]. Accompanying images obtained by 3D Cherenkov-second-harmonic-generation (CSHG) microscopy, our standard nondestructive and real-space method of choice both for visualizing ferroelectric DWs [3,31,32] and especially for correlating their local inclination to the DW conductivity, indeed elucidates a very different DW appearance for $LNO_1$ and $LNO_2$ [see Figs. 1(a) and 1(c)], with average inclination angles between 0° and 0.5° and broad inclination distributions. The two different enhancement procedures for $LNO_1$ and $LNO_2$ are clearly reflected in the two CSHG-microscopy pictures in Figs. 1(a) and 1(c), where the walls in $LNO_2$ show, on average, a much larger distribution of angles, suggesting a larger local screening charge, which is later reflected in the carrier densities; nonetheless, the overall DW conductivities could be readily enhanced for both cases, by 3 orders of magnitude ($LNO_1$) and 6 orders of magnitude ($LNO_2$) at maximum [see Figs. S2(a) and S2(b) as well as Table S1 in Supplemental Material [28] ]. The detailed current-voltage characteristics recorded between the different electrode pairs can be found in Sec. A in Supplemental Material [28].

### C. Realization of Hall-voltage measurements

To quantify the LNO DW Hall voltage, the adapted vdP configuration [24] was used as illustrated in the inset in Fig. 2 and, in a previous study, successfully tested for 2D electron gases in $BaTiO_3$ CDWs [5]. The sample therefore was mounted in an electromagnet at room temperature that delivers magnetic fields $B$ of up to ±420 mT. Contacts 1 and 4 were connected to the Keithley 6517B electrometer to apply a bias voltage of 6 V, which resulted in a domain-wall current $I = I_{14}$ on the order of 0.1 nA. The corresponding carriers hence experience the Lorentz force $F_L$ as sketched in the inset in Fig. 2, resulting in the Hall voltage $U_H := U_{23}$ that is detected between contacts 2 and 3 with a Keithley 2700 multimeter. The ratio $R_h = U_H/I$, subsequently denoted as the Hall resistance, was determined for six different magnetic field values set between 330 and 420 mT. To account for any sample misalignment within the electromagnet (i.e., nonparallel alignment of the magnetic field and DW normal vector), the magnetic field direction was switched by our changing the sign of the electromagnet's voltage, and the measurement series was repeated—a common practice for Hall-voltage measurements [33]. The corresponding dataset was acquired for DW samples $LNO_1$ and $LNO_2$ (see Fig. 2 for the averaged data and Fig. S5 in Supplemental Material [28] for the raw data, i.e., the magnetic-field-direction-dependent data).

TABLE I. Overview of the DW parameters, i.e., the sheet resistance $R_S$ (for the graphical determination see Table S3 and Fig. S4 in Supplemental Material [28]), the 2D charge-carrier density $n_{2D}$, and the Hall mobility $\mu_H$, as extracted from DW-confined Hall-effect measurements with use of Eqs. (1)–(3).

| Sample | $R_S$ ($10^{12}\Omega/\square$) | $n_{2D}$ ($10^3/\mathrm{cm}^2$) | $\mu_H$ ($\mathrm{cm}^2/\mathrm{V\,s}$) |
|---|---|---|---|
| $LNO_1$ | 5.6 | $20 \pm 2$ | $54 \pm 5$ |
| $LNO_2$ | 0.6 | $297 \pm 36$ | $35 \pm 4$ |

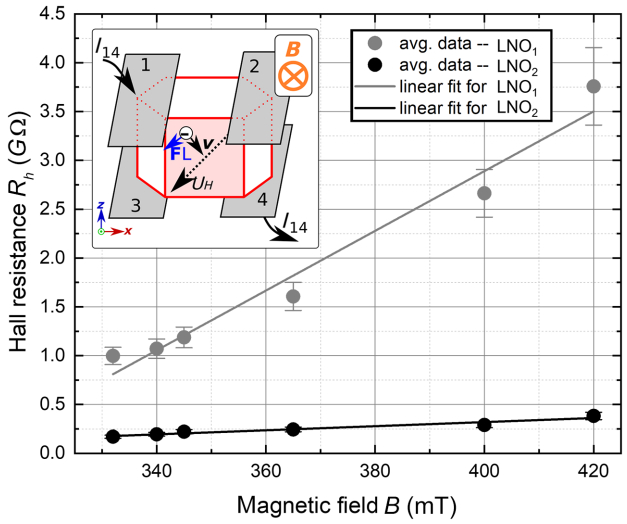


FIG. 2. Results of the macroscopic Hall-effect measurements for $LNO_1$ and $LNO_2$, performed as sketched in the inset. The magnetic field $B$ was applied perpendicular to the CDWs and then swept both positively and negatively. The charge carriers, i.e., mainly electrons—as discussed in the main text—that flow between current contacts 1 and 4 are deflected by the Lorentz force $F_L$, resulting in a measurable Hall voltage $U_H = U_{23}$ read between contacts 2 and 3. Plotted in the main diagram is the Hall resistance $R_h = U_{23}/I_{14}$ as a function of the magnetic field for the two samples, with $LNO_2$ showing a nearly 10 times larger response. Note that the plotted $R_h$ values are the averaged values of $R_h(+B)$ and $R_h(-B)$ so as to compensate for sample misalignment effects (see the raw data in Fig. S5 and the reference $U_H$ measurement recorded from a monodomain bulk LNO crystal (containing no CDW at all) in Fig. S6(a) in Supplemental Material [28]). The corresponding 2D charge-carrier densities $n_{2D}$ were then extracted from the slope of these linear relationships according to Eq. (1) and are discussed further in the main text and are summarized in Table I.

### D. Angular dependence of the Hall voltage

To verify that a true Hall voltage and not a parasitic quantity is measured, the angular dependence $U_H(\Phi)$ was recorded next, by our mounting $LNO_2$ on a rotation table inside the electromagnet. Here, $\Phi$ denotes the angle between the magnetic field vector **B** and the plane of carrier transport, varying between 0° and 90° in a cosine fashion [see the inset in Fig. 3(a)]. $U_H(\Phi)$ was then recorded for a fixed magnetic field of 400 mT at five different $\Phi$ values, including 0° and 90°. The data are plotted in Fig. 3(a), and clearly show the expected Hall-voltage behavior, especially with also $U_H(\Phi = 90°) = 0$ recorded.

### E. Hall voltage under super-band-gap illumination

A second independent integrity experiment, performed also only with $LNO_2$, investigated the influence of super-band-gap illumination on the DW current, which is expected to significantly increase the sheet carrier density $n_{2D}$ by generating electron-hole pairs that then must decrease $R_h$ and $U_H$. For this complementary test, the DW of $LNO_2$ was placed in a 110-mT field of a permanent magnet with $\Phi = 0°$ and then illuminated at a wavelength of 310 nm, which corresponds to the optical band gap $E_g = 4.0$ eV for bulk 5 mol% Mg–doped $LiNbO_3$ [25]. A 1000-W Xe arc lamp coupled to a grating monochromator (Cornerstone 260 from Oriel Instruments) and the light from which was focused onto the whole $5 \times 10$ mm$^2$ sample area served as the photoexciting light source applying a constant photon flux of $10^{13}$ s$^{-1}$ [see the sketch in Fig. 3(b)]. Using this setup, we acquired $U_H$ as a function of DW current $I$ both with and without light. The data are displayed in Fig. 3(b).

### F. Theoretical background for the extraction of sheet carrier densities and Hall mobilities

Before discussing the results of these experiments, we briefly summarize here the mathematical background that is needed to extract both the charge carrier densities $n_{2D}$ and the Hall mobilities $\mu_H$ from our experimental data. A full step-by-step discussion is given in Beccard *et al.* [5], where we underlined the indispensable necessity for offset and error corrections in vdP experiments as outlined by Werner [33]. To interpret our Hall data, we assume that the DW current is established by electrons as the majority charge carriers. That the majority carriers are negative was derived from a preliminary experiment testing simply the polarity of the Hall voltage. The assumption that these carriers are very probably electrons is derived from two recent studies: first, via *in situ* strain experiments for a set of equivalently prepared DWs based on crystal pieces of LNO wafers from the same manufacturer [34] and that electrons are the dominating charge carrier can be understood due to their superior mobility compared with holes and the positive bound charges at a head-to-head DW requiring negative screening charges [26,35]; and second, via temperature-dependent DWC measurements revealing activation energies in the range of 100–250 meV [36] and thus pointing towards electron-polaron-mediated hopping with ionic transport being very improbable. We also assume that the magnetic field is perpendicular to the conductive layer, i.e., the CDW. Then the Hall voltage $U_H$ follows [37,38] the relationship $U_H = IB/qnd$, where $B$ is the absolute value of the magnetic field, $I$ is the current driven through the conducting DW layer (in particular, $I = I_{14}$), $q$ is the elementary charge, $d$ is the DW width, and $n$ is the 3D charge-carrier density. Introducing the 2D charge-carrier density $n_{2D}$, also referred to as the sheet carrier density, with $n_{2D} = nd$ and the Hall resistance $R_h = U_H/I = U_{23}/I_{14}$, one can extract the former from the slope of the (measured) expected linear $R_h$-versus-$B$

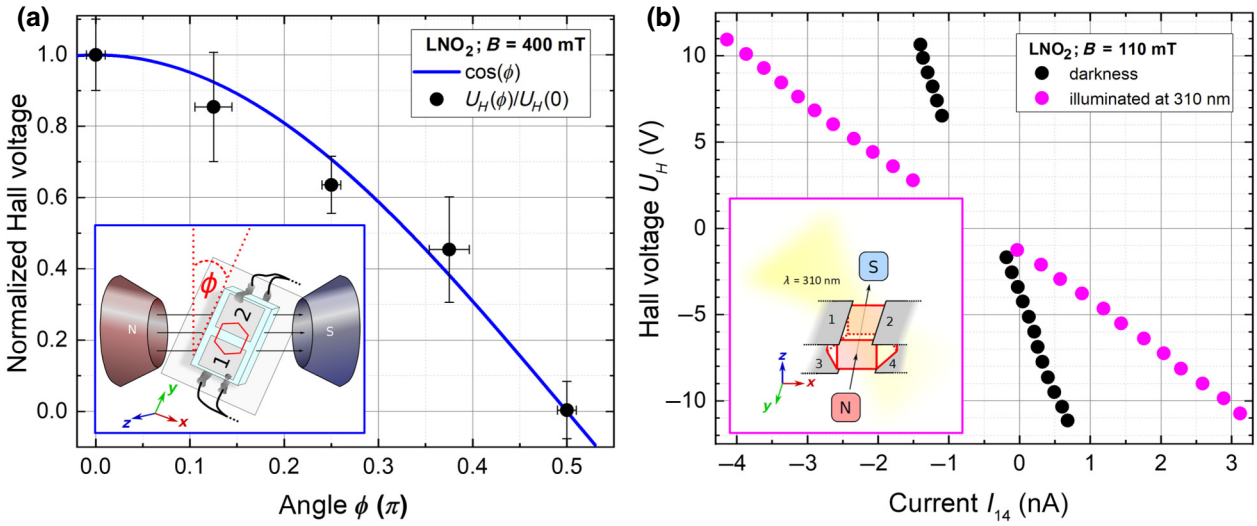


FIG. 3. (a) The DW of $LNO_2$ was exemplarily rotated in the magnetic field of the electromagnet, with the angle $\Phi$ being varied between 0° and 90° and the corresponding Hall voltages measured, as sketched in the inset. As expected, the Hall voltage $U_H$ decreases when $\Phi$ is changed from 0° to 90° and the ratio $U_H/U_{H,0}$ with $U_{H,0}$ being the Hall voltage at 0° (i.e., with the magnetic field vector being aligned perpendicular to both the CDW and the injected current) follows the theoretically predicted cosine function very clearly. All data points were acquired with a constant magnetic field of 400 mT. (b) Impact of super-band-gap illumination on the Hall transport for $LNO_2$, which was placed in a constant magnetic field of 110 mT supplied by a permanent magnet and illuminated at a wavelength of 310 nm under a constant photon flux of $10^{13}$ $s^{-1}$. The Hall voltage $U_H = U_{23}$ was recorded as a function of the current $I = I_{14}$ for the two cases: (i) under illumination (purple data points) and (ii) in the dark (black data points). Both datasets show a linear behavior, however with a significantly increased response when the DW is illuminated, then generating additional electron-hole pairs.

dependence as

$$R_h \propto \frac{B}{qn_{2D}}. \tag{1}$$

For the subsequent calculation of the Hall mobility $\mu_H$ of the majority charge carriers, we use the relation

$$\mu_H = \frac{1}{qn_{2D}R_S}. \tag{2}$$

Note that the Hall mobility $\mu_H$ is linked to the "actual" mobility $\mu$ via the Hall factor $R_h$ as $\mu_H = R_h\mu$. The Hall factor, which depends on internal scattering mechanisms, is not known in most practical cases and is commonly assumed to be unity [20]. Furthermore, $R_S$ is the sheet resistance of the CDW, which is readily obtained by solving the van der Pauw equation numerically [38]:

$$\exp\left(-\frac{\pi}{R_S}R_{13,42}\right) + \exp\left(-\frac{\pi}{R_S}R_{34,21}\right) = 1. \tag{3}$$

$R_{13,42} = U_{42}/I_{13}$ and $R_{34,21} = U_{21}/I_{34}$ are easily extracted from corresponding current-injection and voltage measurements between the respective contacts. The values measured here are listed in Table S3 in Supplemental Material [28].

## III. RESULTS AND DISCUSSION

As key findings of our study, the measured relationship between $R_h = U_H/I$ and the absolute value of the magnetic field $B$ normal to the DW is depicted for both DWs in Fig. 2. The corresponding raw data before averaging over both field directions are shown in Fig. S5 in Supplemental Material [28], while an additional averaging over the two possible current directions as in Refs. [5,33] could not be realized due to the rectifying character of the $U_{23}$-versus-$I_{14}$ curves. According to Eq. (1), rewritten as $R_h \propto bB$, with slope $b = 1/qn_{2D}$, very clear and linear dependencies of the $R_h$-versus-$B$ curves are indeed observed experimentally here for the DWs in both LNO samples. The corresponding slopes were extracted from the linear fits. They read as $b_1 = (31 \pm 3) \times 10^9\ \Omega\,T^{-1}$ and $b_2 = (21 \pm 3) \times 10^8\ \Omega\,T^{-1}$ for $LNO_1$ and $LNO_2$, respectively. Table I summarizes the sheet carrier densities $n_{2D}$ as extracted from these slopes. The numerical values of $n_{2D}$ cover 2 orders of magnitude for the two samples, with $LNO_2$ showing the larger $n_{2D}$ value of $3 \times 10^5$ $cm^{-2}$, which is 2 orders of magnitude larger than the value recently observed in conductive $BaTiO_3$ DWs, and, moreover, is a very-reasonable value for a 2D electronic system [5]. Reconsidering the findings of the CSHG imaging [see Figs. 1(a) and 1(c)] the $n_{2D}$ discrepancy between $LNO_1$

and $LNO_2$ is not a surprise, since the DW of $LNO_2$ shows a broader range of DW inclination angles. Consequently, a greater charge-carrier reservoir in contrast to $LNO_1$ is obviously expected. In other words, the link between DW geometry, or more generally, the DW's real structure, and electrical performance is reflected in the present Hall-effect results.

In principle, the 3D charge-carrier density $n = n_{2D}/d$ can be calculated as well, provided the DW width $d$ is known. Nevertheless, for the two samples here, $d$ is unknown, but to tentatively estimate typical values we use the literature value of 174 pm, which was derived by transmission electron microscopy by Gonnissen *et al.* [39] on macroscopically noninclined LNO domain walls, and obtain carrier densities $n$ of $1.15 \times 10^{12}$ $cm^3$ for $LNO_1$ and $17 \times 10^{12}$ $cm^3$ for $LNO_2$. However, it is currently not clear (i) whether the width of our conductivity-enhanced DWs here is comparable with the width of the DWs as measured by Gonnissen *et al.* and (ii) to what extent the width of the transport channel is different from the width defined by the polarization change as measured via transmission electron microscopy, i.e., whether screening charges are trapped in a larger area. Therefore, the above values for $n$ should be seen as first "qualified guesses."

The second quantity evaluated from our four-point-probe setup using Eqs. (2) and (3) is the Hall mobility $\mu_H$. The extracted values are listed in Table I. In comparison with mobilities of LNO *bulk* that have been reported [40] to be 0.8 $cm^2/V\,s$, the *domain walls'* Hall mobilities found here are significantly (almost 2 orders of magnitude) higher, which is an expected and desirable result. On the other hand, the Hall mobilities in *thin-film-based*-LNO domain walls, which were reported by Qian *et al.* [22] (337.30 $cm^2/V\,s$) and McCluskey *et al.* [23] (around 3700 $cm^2/V\,s$) are 1–2 orders of magnitude larger once more and it will be a future experimental challenge to investigate whether these ranges can be achieved within LNO-single-crystal DWs as well. One may question to what extent the preconditions that justify Eq. (3) are satisfied for the DWs of the current study. In an ideal case, the conducting sheet in the van der Pauw configuration has to be homogeneous, isotropic, uniform in thickness, and without holes, and the contacts have to be point contacts at the perimeter. Reconsidering the CSHG-microscopy images showing a significant range of inclination angles and a tendency towards spike-domain formation at least for $LNO_2$ and the fact that the LNO DWs are more tube-like rather than forming a 2D sheet, we find that it appears to be necessary to estimate these errors as induced by these nonidealities:

In the simplest case and as indicated in Figs. 1(b) and 1(d), the Hall transport in $LNO_1$ and $LNO_2$ can be assumed as a parallel conduction through two identical DW sheets, which would mean a factor of 2 between the measured current and the current flowing through one of the two sheets, i.e., in turn, $n_{2D}$ would be diminished by a factor of 2. Accounting for the more-complex real structure of the CDWs in $LNO_1$ and $LNO_2$ [see Figs. 1(a) and 1(c)], we performed resistor-network simulations as described in detail earlier [27] and briefly outlined in Sec. D in Supplemental Material [28], with the rather-similar result that the determined charge-carrier densities are of the same order of magnitude needing correction factors of 0.51 and 0.65 for $LNO_1$ and $LNO_2$, respectively (Sec. D in Supplemental Material [28]). Note that the other extreme case, i.e., a strongly asymmetric conductivity of the two parallel DW sheets, would not need such a correction, since the measurement would reflect mainly the "Hall behavior" of the highly conductive DW. Against the background that in a Hall scenario primarily the *orders of magnitude* of the carrier densities and mobilities are of interest, correction factors between 0.5 and 1 are fully acceptable in any case.

Nevertheless, the nonideal fitting to the van der Pauw restrictions gave further motivation for use to test the integrity of the approach by additional Hall-effect measurements.

In a first supporting experiment we recorded the dependence of $U_H$ on the angle $\Phi$ enclosed by the magnetic field $B$ and conducting sheet as exemplarily illustrated in Fig. 3(a) for $LNO_2$, i.e., the DW with the largest charge-carrier density and the lowest sheet resistance. As seen from the plot of the normalized Hall voltage $U_H/U_{H,0}$ versus angle $\Phi$, the expected cosine behavior is convincingly reproduced by the measured data.

In a second additional experiment, illustrated in Fig. 3(b), performed again with the DW of $LNO_2$, we studied whether super-band-gap illumination at 310 nm, which corresponds to the optical band gap of Mg-doped $LiNbO_3$ of 4.0 eV, might impact the Hall voltage. The earliest experiments focusing on measuring the DW conductivity in LNO qualitatively reported that super-band-gap light strongly increases the charge-carrier density at DWs [25]. Indeed, the slope of the $U_H$-versus-$I$ curve decreases under UV illumination, as shown in Fig. 3(b), indicating a decrease in $R_h$ and hence an increase in the sheet carrier density $n_{2D}$, as follows from Eq. (1). The numerical evaluation of the slope via linear curve fitting yields a significant increase of the carrier density by a factor of 4–5 under super-band-gap excitation with a rather moderate photon flux. In the control experiment where a monodomain $z$-cut $LiNbO_3$ bulk crystal (i.e., without hexagonal domain structures) was covered with the same electrode configuration and tested in the same type of measurement scenario, a bulk photoinduced Hall effect could be excluded, since no functional relationship between the driving current $I_{14}$ and the Hall voltage $U_{23}$ apart from noise was observed [Fig. S6(b) in Supplemental Material [28] ]. Thus, we state that the proposed Hall-effect measurement setup is also efficient for investigating the photoinduced DW-confined transport behavior, which clearly

opens up the box to implement DW-based devices for nano-optoelectronic applications as well.

## IV. CONCLUSION

In summary, two exemplary ferroelectric conductive domain walls, engineered into a $z$-cut 200-μm-thick 5 mol% MgO–doped $LiNbO_3$ single crystal, completely penetrating the latter and shaped like hexagonal tubes with, however, a different microscopic real structure, were macroscopically electrically connected with four Cr electrodes (two on the $z^+$ surface and two on the $z^-$ surface) to set up a van der Pauw four-point-probe geometry for Hall probing. This setting in turn was used to measure the Hall resistance $R_h$ as a function of the magnetic field $B$ applied perpendicular to two of the six side sheets of the hexagonally shaped DW tubes, as well as the sheet resistance $R_s$ of the DWs, which finally allowed us to extract two characteristic key quantities for such low-dimensional electronic systems, i.e., the 2D charge-carrier density $n_{2D}$, which was found to be in the range from $20 \times 10^2$ to $300 \times 10^2$ $cm^{-2}$, and the Hall mobility $\mu_H$ (extracted as 54 and 35 $cm^2/V\,s$ for the two samples, respectively, with a reasonable error of around 10%). The validity of these numbers was further tested through angle- and illumination-dependent Hall-voltage recordings, which both showed the expected behavior. Moreover, we used resistor-network simulations to calculate correction factors for $n_{2D}$ and $\mu_h$, due to the parallel junction formed by the two CDWs, which were in the range of 0.5 and thus did not change the order of magnitude of the two quantities. Thus, we propose that macroscopic Hall-effect analysis, as applied here, provides a robust and versatile method for the comparative quantification of the electrical performance of conductive domain walls in both LNO and many other materials. Moreover, photoinduced-Hall-effect measurements might gain even more interest, especially also for realizing nano-optoelectronic circuits.

The data that support the findings of this study are available from the corresponding author upon reasonable request.

## ACKNOWLEDGMENTS

We acknowledge financial support by the Deutsche Forschungsgemeinschaft (DFG) through the joint DFG-ANR project TOPELEC (EN 434/41-1 and ANR-18-CE92-0052-1), Collaborative research Center (CRC) 1415 (ID 417590517), FOR 5044 (ID 426703838), and the Würzburg-Dresden Cluster of Excellence on "Complexity and Topology in Quantum Matter"—ct.qmat (EXC 2147, ID 39085490). This work was supported by the Light Microscopy Facility, a core facility of the CMCB Technology Platform at Technische Universität Dresden.

[1] K. S. Novoselov, A. Mishchenko, A. Carvalho, and A. H. C. Neto, 2D materials and van der Waals heterostructures, Science **353**, aac9439 (2016).

[2] C. Godau, T. Kämpfe, A. Thiessen, L. Eng, and A. Haußmann, Enhancing the domain wall conductivity in lithium niobate single crystals, ACS Nano **11**, 4816 (2017).

[3] B. Kirbus, C. Godau, L. Wehmeier, H. Beccard, E. Beyreuther, A. Haußmann, and L. Eng, Real-time 3D imaging of nanoscale ferroelectric domain wall dynamics in lithium niobate single crystals under electric stimuli: Implications for domain-wall-based nanoelectronic devices, ACS Appl. Nano Mater. **2**, 5787 (2019).

[4] T. Sluka, A. Tagantsev, P. Bednyakov, and N. Setter, Free-electron gas at charged domain walls in insulating $BaTiO_3$, Nat. Commun. **4**, 1808 (2013).

[5] H. Beccard, B. Kirbus, E. Beyreuther, M. Rüsing, P. Bednyakov, J. Hlinka, and L. M. Eng, Nanoscale conductive sheets in ferroelectric $BaTiO_3$: Large Hall electron mobilities at head-to-head domain walls, ACS Appl. Nano Mater. **5**, 8717 (2022).

[6] M. Rusing, P. O. Weigel, J. Zhao, and S. Mookherjea, Toward 3D integrated photonics including lithium niobate thin films: A bridge between electronics, radio frequency, and optical technology, IEEE Nanotechnol. Mag. **13**, 18 (2019).

[7] D. Zhu, L. Shao, M. Yu, R. Cheng, B. Desiatov, C. J. Xin, Y. Hu, J. Holzgrafe, S. Ghosh, A. Shams-Ansari, E. Puma, N. Sinclair, C. Reimer, M. Zhang, and M. Lončar, Integrated photonics on thin-film lithium niobate, Adv. Opt. Photonics **13**, 242 (2021).

[8] D. Sun, Y. Zhang, D. Wang, W. Song, X. Liu, J. Pang, D. Geng, Y. Sang, and H. Liu, Microstructure and domain engineering of lithium niobate crystal films for integrated photonic applications, Light Sci. Appl. **9**, 197 (2020).

[9] T. Kämpfe, B. Wang, A. Haußmann, L.-Q. Chen, and L. M. Eng, Tunable non-volatile memory by conductive ferroelectric domain walls in lithium niobate thin films, Crystals **10**, 804 (2020).

[10] G. Catalan, J. Seidel, R. Ramesh, and J. F. Scott, Domain wall nanoelectronics, Rev. Mod. Phys. **84**, 119 (2012).

[11] D. Meier, Functional domain walls in multiferroics, J. Condens. Matter Phys. **27**, 463003 (2015).

[12] T. Sluka, P. Bednyakov, P. Yudin, A. Crassous, and A. Tagantsev, in *Topological Structures in Ferroic Materials: Domain Walls, Vortices and Skyrmions*, edited by J. Seidel (Springer International Publishing, Cham, 2016), p. 103.

[13] P. S. Bednyakov, B. I. Sturman, T. Sluka, A. K. Tagantsev, and P. V. Yudin, Physics and applications of charged domain walls, Npj Comput. Mater. **4**, 65 (2018).

[14] P. Sharma, P. Schoenherr, and J. Seidel, Functional ferroic domain walls for nanoelectronics, Materials **12**, 2927 (2019).

[15] G. Nataf, M. Guennou, J. Gregg, D. Meier, J. Hlinka, E. K. H. Salje, and J. Kreisel, Domain-wall engineering and topological defects in ferroelectric and ferroelastic materials, Nat. Rev. Phys. **2**, 634 (2020).

[16] D. Meier and S. Selbach, Ferroelectric domain walls for nanotechnology, Nat. Rev. Mater. **7**, 157 (2021).

[17] P. Sharma, T. S. Moise, L. Colombo, and J. Seidel, Roadmap for ferroelectric domain wall nanoelectronics, Adv. Funct. Mater. **32**, 2110263 (2022).

[18] B. M. Vul, G. M. Guro, and I. I. Ivanchik, Encountering domains in ferroelectrics, Ferroelectrics **6**, 29 (1973).
[19] E. Eliseev, A. Morozovska, G. Svechnikov, V. Gopalan, and V. Y. Shur, Static conductivity of charged domain walls in uniaxial ferroelectric semiconductors, Phys. Rev. B **83**, 235313 (2011).
[20] M. Campbell, J. McConville, R. McQuaid, D. Prabhakaran, A. Kumar, and J. Gregg, Hall effect in charged conducting ferroelectric domain walls, Nat. Commun. **7**, 13764 (2016).
[21] P. Turner, J. McConville, S. McCartan, M. Campbell, J. Schaab, R. McQuaid, A. Kumar, and J. Gregg, Large carrier mobilities in $ErMnO_3$ conducting domain walls revealed by quantitative Hall-effect measurements, Nano Lett. **18**, 6381 (2018).
[22] Y. Qian, Y. Zhang, J. Xu, and G. Zhang, Domain-wall *p*-*n* junction in lithium niobate thin film on an insulator, Phys. Rev. Appl. **17**, 044011 (2022).
[23] C. J. McCluskey, M. G. Colbear, J. P. V. McConville, S. J. McCartan, J. R. Maguire, M. Conroy, K. Moore, A. Harvey, F. Trier, U. Bangert, A. Gruverman, M. Bibes, A. Kumar, R. G. P. McQuaid, and J. M. Gregg, Ultrahigh carrier mobilities in ferroelectric domain wall Corbino cones at room temperature, Adv. Mater. **34**, 2204298 (2022).
[24] L. van der Pauw, A method of measuring the resistivity and hall coefficient on lamellae and arbitrary shape, Philips Tech. Rev. **20**, 220 (1958).
[25] M. Schröder, A. Haußmann, A. Thiessen, E. Soergel, T. Woike, and L. Eng, Conducting domain walls in lithium niobate single crystals, Adv. Funct. Mater. **22**, 3936 (2012).
[26] C. Werner, S. Herr, K. Buse, B. Sturman, E. Soergel, C. Razzaghi, and I. Breunig, Large and accessible conductivity of charged domain walls in lithium niobate, Sci. Rep. **7**, 9862 (2017).
[27] B. Wolba, J. Seidel, C. Cazorla, C. Godau, A. Haußmann, and L. Eng, Resistor network modeling of conductive domain walls in lithium niobate, Adv. Electron. Mater. **4**, 1700242 (2018).
[28] See Supplemental Material at http://link.aps.org/supplemental/10.1103/PhysRevApplied.20.064043 for current-voltage characteristics, Hall-effect raw data, graphical determination of sheet resistances, and polarization-sensitive-microscopy images of the domain walls, as well as resistor-network simulation details.
[29] M. Wengler, U. Heinemeyer, E. Soergel, and K. Buse, Ultraviolet light-assisted domain inversion in magnesium-doped lithium niobate crystals, J. Appl. Phys. **98**, 064104 (2005).
[30] I. Kiseleva, Master's thesis, Technische Universität Dresden, 2023. https://nbn-resolving.org/urn:nbn:de:bsz:14-qucosa2-876252.
[31] T. Kämpfe, P. Reichenbach, M. Schröder, A. Haußmann, L. Eng, T. Woike, and E. Soergel, Optical three-dimensional profiling of charged domain walls in ferroelectrics by cherenkov second-harmonic generation, Phys. Rev. B **89**, 035314 (2014).
[32] T. Kämpfe, P. Reichenbach, A. Haußmann, T. Woike, E. Soergel, and L. Eng, Real-time three-dimensional profiling of ferroelectric domain walls, Appl. Phys. Lett. **107**, 152905 (2015).
[33] F. Werner, Hall measurements on low-mobility thin films, J. Appl. Phys. **122**, 135306 (2017).
[34] E. Singh, H. Beccard, Z. H. Amber, J. Ratzenberger, C. W. Hicks, M. Rüsing, and L. M. Eng, Tuning domain wall conductivity in bulk lithium niobate by uniaxial stress, Phys. Rev. B **106**, 144103 (2022).
[35] S. Y. Xiao, T. Kämpfe, Y. M. Jin, A. Haußmann, X. M. Lu, and L. M. Eng, Dipole-tunneling model from asymmetric domain-wall conductivity in $LiNbO_3$ single crystals, Phys. Rev. Appl. **10**, 034002 (2018).
[36] M. Zahn, E. Beyreuther, I. Kiseleva, A. S. Lotfy, C. J. McCluskey, J. R. Maguire, A. Suna, M. Rüsing, J. M. Gregg, and L. M. Eng, R2D2—an equivalent-circuit model that quantitatively describes domain wall conductivity in ferroelectric $LiNbO_3$, arXiv:2307.10322 (2023).
[37] D. K. Schroder, *Semiconductor Material and Device Characterization* (Wiley-VCH, Hoboken, New Jersey, 2006).
[38] M. Lundstrom, *Fundamentals of Carrier Transport* (Cambridge University Press, Cambridge, 2000).
[39] J. Gonnissen, D. Batuk, G. F. Nataf, L. Jones, A. M. Abakumov, S. Van Aert, D. Schryvers, and E. K. H. Salje, Direct observation of ferroelectric domain walls in $LiNbO_3$: Wall-meanders, kinks, and local electric charges, Adv. Funct. Mater. **26**, 7599 (2016).
[40] Y. Ohmori, M. Yamaguchi, K. Yoshino, and Y. Inuishi, Electron Hall mobility in reduced $LiNbO_3$, Jpn. J. Appl. Phys. **15**, 2263 (1976).